

Strong Field Population Control: Theory and Experiment

6.1 Introduction

Ultrafast lasers have come to be used all over the world to study chemical and physical dynamics on the shortest of timescales. With the short timescales inherent to ultrafast lasers often comes high peak laser power. This can sometimes be problematic, since a system response to a strong field, such as that produced for a short time by an ultrafast laser, can cause interesting, or confounding, effects. Among these effects are multiphoton absorption[6, 20, 23], transition saturation effects[66], ultrashort X-ray generation[26, 67], or even nuclear fusion[68, 69]. Before the advent of ultrafast lasers, studies into strong field dynamics with nanosecond lasers have illuminated several of the same processes now also observed by ultrafast lasers[5], and there have even been examples of coherent control using cw lasers[36].

The study of wave packet dynamics and coherent control has a fairly broad base with respect to weak field processes where the outcomes are conveniently described using perturbation theory[9, 12, 17, 18, 70, 71]. There is a well established formalism for describing the response of molecules in the stronger field regime using the dressed state approach[36]. Somewhere in between these two regimes lies what would be considered stronger than perturbative, but which is not conveniently described using the dressed state approach. This chapter will investigate this middle ground, first theoretically and then experimentally.

One of the major goals of the analyses and experiments described here is to verify the complete depopulation of a single state in a molecule. This has been shown in many types of regimes, with and without pulse shaping[5, 36, 72]. Besides dynamic processes such as population inversion in lasers, stable population inversion can be seen in isolated systems with the application of a single pulse, producing Rabi oscillations in an excited state population[5]. Besides simple atomic systems, this effect has been observed or predicted in complex systems such as semiconductor quantum dots or molecules[52, 73]. With a little bit higher fields and even rudimentary pulse shaping, full population transfer to an excited state via Rapid Adiabatic Passage or to a third state with stimulated Raman via adiabatic passage (STIRAP) has been demonstrated on numerous systems[36, 66, 72, 74-79]. Often, in these cases, the systems are characterized by a single resonance or a series of resonances that are well separated in energy.

One way the theory and experiments in this chapter will expand upon this previous groundwork is that all transitions are embedded within the spectrum of a single broadband laser pulse, introducing a level of richness only recently addressed[23, 75, 80, 81]. Another is that these experiments are rotationally resolved, allowing a precise level of bookkeeping. Since the theory and experiments described here focus on second and third order coherences (*i. e.* involving two or three photons, respectively), some similar types of coherences can be created using various four wave mixing techniques[39, 82]. Two traits separate these experiments, however. First, these experiments will show evidence

for a *depopulation* of states, and second, these methods can be extended to study an arbitrary order of coherence without any intrinsic changes in methodology.

The successful development of this higher order pumping could be a means for easily selecting rotational quanta by coherent control. It is also a good model system for studying moderately dispersed processes such as population transfer among several vibrational states in a real molecule[24, 83, 84]. In fact, the system described here simply represents the dynamics at play for a single rotational state in a typical ground state ensemble—this study provides a basis for understanding the limitations of population transfer within an ensemble of rotational states. The techniques described in this chapter create what is essentially a rotational analog to vibrational ladder climbing[72, 78, 84-87]. In essence, the lessons learned here can eventually be used to generate highly excited rotational states, but with state specificity. One other important application of the lessons learned here is the potential for manipulating quantum information systems. In some material systems (such as trapped ions), series of unshaped population inverting pulses are used to switch qubit states, but an alternate method of population switching based upon ladder climbing with chirped pulses is presented here[63].

This chapter will only focus on the requirements that need to be met to measure state-resolved population transfer. We study an optically coupled system consisting of a progression of J values for a single vibrational level on each of two electronic states, so that the total wavefunction consists of a superposition of optically excited J states on the $A^1\Sigma_u^+$ and $E^1\Sigma_g^+$ electronic potential energy

curves. Experimentally, to measure populations, quantum beating between states will act as the primary sensor. One difficulty with excitation by higher fields is that the strong excitations on a theoretically isolated system may induce *too many* transitions. To see state resolved population transfer within the coupled system requires that the finite starting population not spread out among many different rotational states in the coupled system via optical pumping. This process of spreading out of wave function via optically induced $\Delta J = \pm 1$ transitions will be referred to as wavefunction dissipation. This wavefunction dissipation reduces the amplitude of a single observed quantum beat between two states since each individual state will have a reduced population, even if no population is lost out of the target coupled system. A second requirement for observation is that population not get optically excited out of the coupled system; this will be referred to as wavefunction depletion since the population in the coupled system decreases. In a molecule exposed to strong field laser pulses, processes such as multiphoton ionization and excitation to continuum states can play a significant role in population losses. Besides dissipation and depletion effects, certain physical phenomena such as the spatial beam profile and molecular alignment make observing oscillations in population as a function of electric field strength difficult[88-90], since these effects introduce inhomogeneities in the overall transition strength.

This chapter will begin with a theoretical treatment of the background issues required to consider strong field dynamics. The first section focuses on calculations related to the effect of field strength on the populations in the coupled

system. The calculations will start with a simple model, with the model complexity increasing step by step to account for experimental nonidealities. It will be shown that as the field strength increases, the degree of dissipation of the population over various J states increases to create a superposition of many J states at surprisingly low field strengths. Next, the influence of a spatially nonuniform electric field, as expected by a Gaussian beam, will be addressed, as well as the effect expected from using a specific probe beam profile. The reduction in the visibility of molecular Rabi oscillations because of alignment effects will also be discussed. Following this theoretical section, the field strength dependence of rotational quantum beats will be analyzed, and an example of wave packet dissipation will be shown. Depletion mechanisms are proposed, and a means to overcome this via spectral filtering is tested. The possibilities of controlling time and field strength dependent dynamics will be considered in both the theoretical and experimental sections with a simple case of implementing a Rapid Adiabatic Transfer Passage (RAP) using a chirped pulse[91], with the secondary goal of finding a population transfer scheme that shows robustness with respect to electric field strength.

6.2 Theory

This section will focus on the interactions between an electric field and two optically coupled progressions of J states. The goal of this theoretical section is to define and then control wavefunction dissipation. First, the theoretical formalism will be established, followed by an analysis of the response to a strong

ultrafast laser pulse of a system with numerous (~15) transitions embedded within the laser bandwidth. Here, the term strong refers to a breakdown of the normal weak field assumption that the population in the launch state remains near unity. Instead, the observed population of the launch state goes through a series of decaying oscillations as the total wavefunction dissipates to larger and larger numbers of J states on the A and E potentials. This will be followed by an analysis of expected trends in electric field strength dependence assuming selected probe pulse characteristics and alignment issues.

6.2.1 Spatially uniform fields

The dynamics used to model the system under the assumption of a spatially uniform laser intensity are summarized below. First, it is assumed that a pure launch state is used ($v_A, J_A=11,28$), as in all previous chapters. Disregarding depletion of the population out of the $A^1\Sigma_u^+(v_A=11)$ and $E^1\Sigma_g^+(v_E=9)$ vibronic states, the time dependent wave function has the following form:

$$\Psi(t) = \frac{\sum_{j=-J_0}^{\infty} c_j(t) |v_j J_j\rangle}{\sum_{j=-J_0}^{\infty} |c_j(t)|^2} \quad (6.1a)$$

where each wavefunction $|v_j J_j\rangle$ represents one of the rovibrational wavefunctions shown in Fig. 6.1, and $c_j(t)$ represents the amplitude of each wavefunction. It is instructive to note that all odd J states are on the E electronic potential, and all even J states are on the A electronic potential. All J quantum numbers are offset relative to the launch state of J=28, so the summations go from -28 to ∞ . To reduce calculation times, the summations are over J=22-34, and P

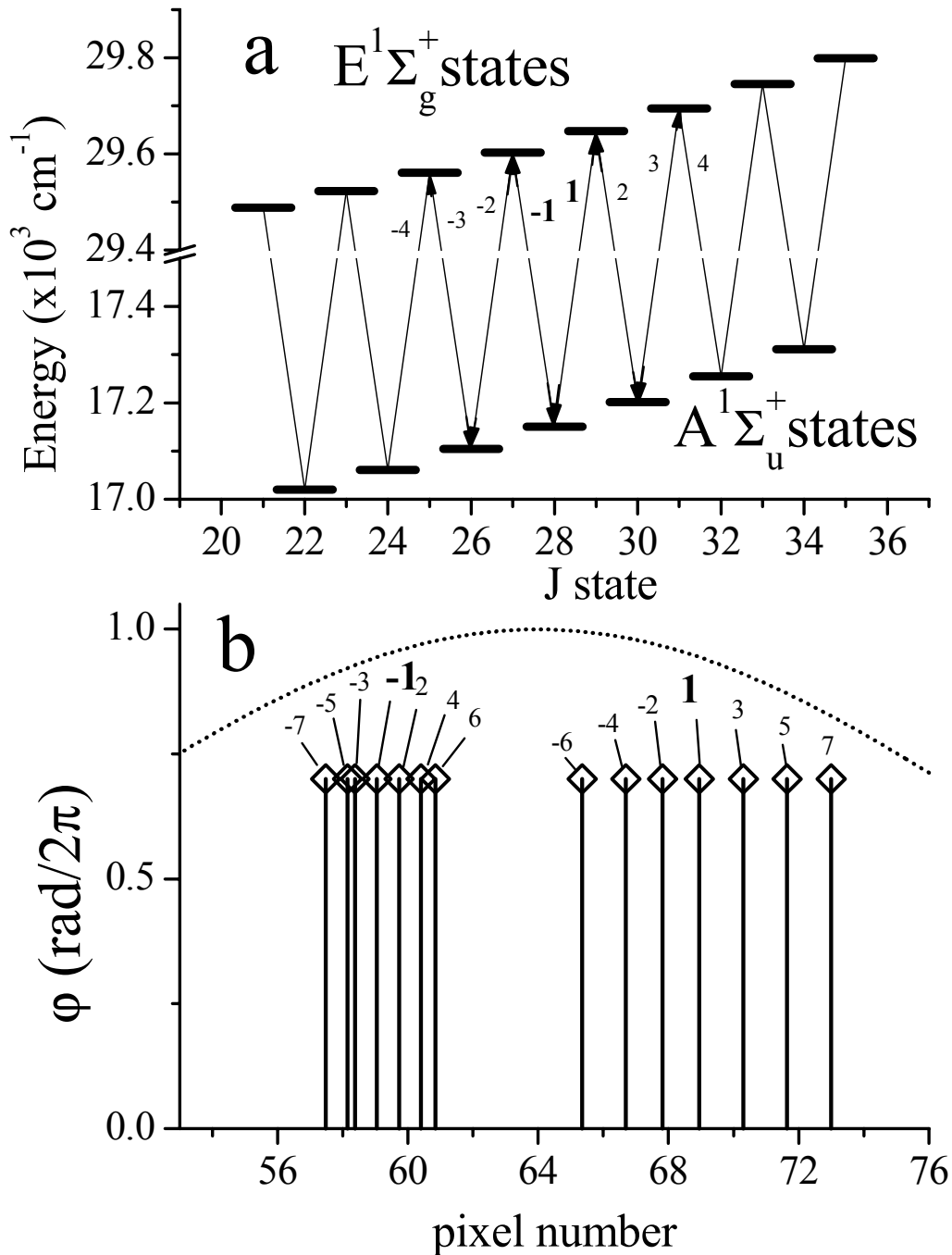


Figure 6.1: Summary of resonant frequency positions. Panel a: Energy levels considered in this theoretical treatment. Resonant transitions are notated by their greatest proximity from the launch state of $J=28$. For example, a transition between $J=31$ & 32 is noted 4 ($32-28=4$) regardless of whether it is a “pump” or “dump” process. Panel b: Resonance locations as imaged onto the SLM. The dotted line represents the Gaussian spectral envelope.

and R branch pump (and dump) transitions are notated relative to their greatest proximity to the $J=28$ state in J space. In all of the calculations presented here, the wavefunction fails to dissipate to the J limit, justifying the J space truncation. Each of the coefficients $c_j(t)$ are calculated as

$$c_j(t) \propto i \int_{-\infty}^{\infty} dt \varepsilon(t) \sum_k c_k(t) \sigma_{jk} e^{i\omega_{jk}t} \quad (6.1b)$$

where the summation is over all states k , $\varepsilon(t)$ is the electric field, σ_{jk} is the transition moment, and ω_{jk} is the resonant frequency between any two of the coupled states. With a typical minimum pulse length of ~ 150 fs compared to the optical cycle of ~ 2.87 fs, the slowly varying envelope approximation is applied, giving a temporally varying electric field as

$$\varepsilon(t) \approx N_{FS} |E(t)| \cos[\omega(t)t + \phi(t)]. \quad (6.1c)$$

where $|E(t)|$ is the pulse envelope, and N_{FS} is a field strength normalization parameter, to be described below. The time dependence of the frequency and the phase has been made explicit to account for pulse shaping situations. Since only P and R branch transitions are strongly allowed between the A and E states, the oscillator strength varies only slightly with J ($< 5\%$ for $m_j=0$)[92], so if we assume that all states are in $m_j=0$, $\sigma_{jk} = \delta(j, k=j\pm 1)$. Following the first few calculations, the m_j dependence of the transition dipole will be made explicit. With the $J_A=28$ launch state, this selection rule establishes that all even J states are on the A state, and all odd J are on the E state. The exploitation of the $\Delta J = \pm 1$ selection rule simplifies the above scheme to 14 coupled differential equations. For a two level system, this dynamical model reduces to the classic Rabi formula:

$$|c_e(t)|^2 = 1 - |c_g(t)|^2 = \int d\Delta \left[1 - \left(\sigma_{eg} \mathcal{E}(\Delta) / \Omega_{eg} \right)^2 \sin^2(\Omega_{eg} t) \right] \quad (6.2a)$$

$$\Omega_{eg} = \sqrt{\Delta^2 + \left[\sigma_{eg} \mathcal{E}(\Delta) \right]^2}, \quad (6.2b)$$

where $\Delta = \omega_{eg} - \omega$ is the detuning away from resonance, and σ_{eg} is the transition moment from the ground to excited state[93].

In the dynamics modeled here, we express the electric field as outlined in the literature[34], and summarized in Eq. (3.1a), with a central wavelength of 801.7 nm and a Gaussian bandwidth of 9 nm, imaged onto the SLM over 35 pixels with a single frequency spot size of 1.7 pixels, with all extents expressed as FWHM (see Fig. 6.1). In many of the calculations and experiments in this chapter, the system dynamics as a function of the normalized field strength, N_{FS} from Eq. (6.1c), are explored. The excitation pulses are normalized so that for a two level system [i.e. $\sigma_{28,29} = 1$, all other $\sigma_{jk} = 0$, see Eq. (6.2)] with an unshaped pulse, the time integrated product of $\mathcal{E}(t)\sigma_{28,29}t = \pi$ holds for $N_{FS} = 1$. The unit N_{FS} is used instead of *pulse area* to avoid confusion with the beam size (see [5]). Given that several of the calculations and experiments involve phase and amplitude shaped pulses, N_{FS} for a shaped pulse is expressed in terms of the unshaped *parent* pulse. This allows the comparison of shaped and unshaped pulses.

In contrast to the two state calculation, when all of the strongly allowed transition moments ($\sigma_{J,J\pm 1}$) are set to 1, the wavefunction will dissipate to an increasing number of rotational states as N_{FS} increases. Figure 6.2 shows the results of this dynamical model as applied to this system for an unshaped input pulse. In this calculation, probe beam and alignment effects have not yet been

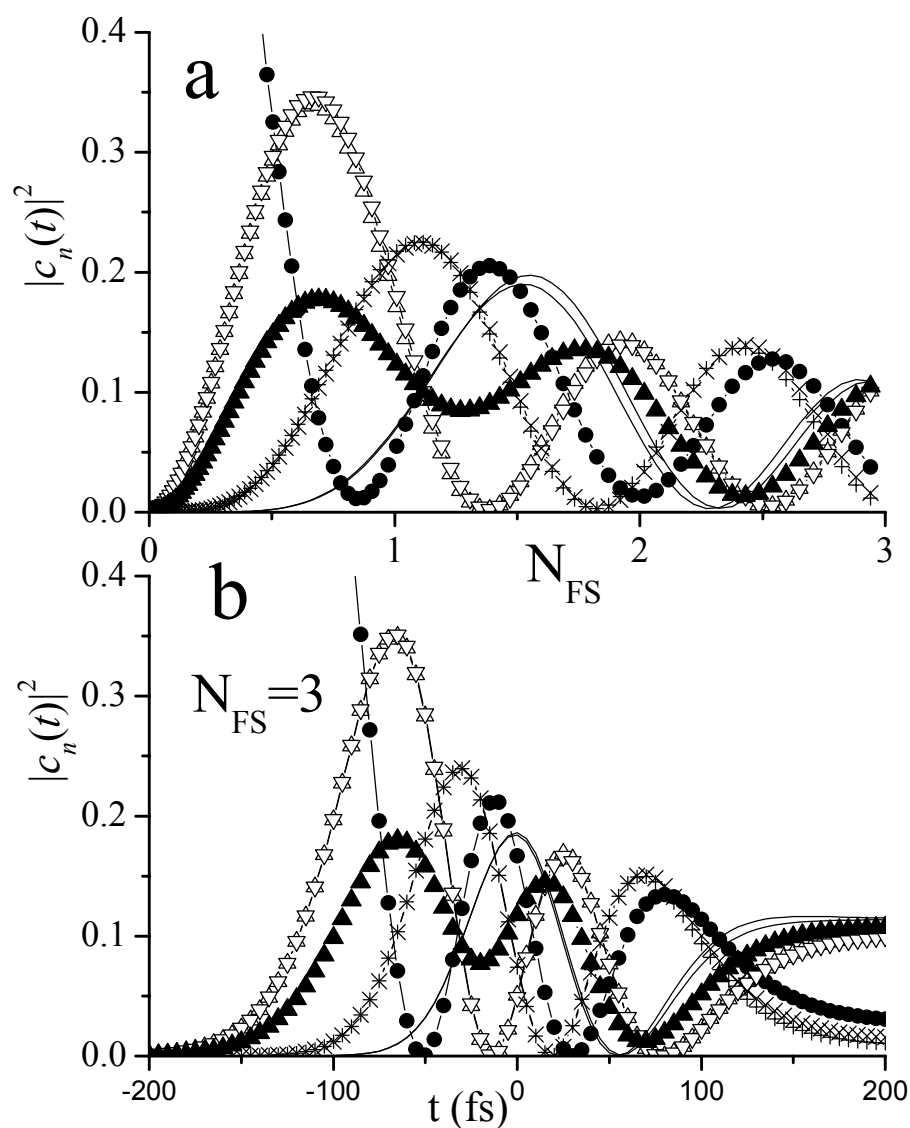


Figure 6.2: Dissipation of wavefunction over various J states for $m_j=0$. An unshaped spectrally Gaussian pulse is used, and the populations are normalized. In both panels, the launch state (●), $\Delta J = \pm 1$ (△, ▽), $\Delta J = \pm 2$ (+, ×), and $\Delta J = \pm 3$ (solid lines) are included, along with the average of the shown E state populations (▲). Panel a: The $t = \infty$ population distribution as a function of field strength normalization parameter N_{FS} . Panel b: The time evolution of the J-state distribution as a function of time for $N_{FS} = 3$. Notice in both panels how states at $+J$ and $-J$ are approximately the same.

implemented. The population transfer in this unshaped case shows similar dynamics as a function of both time and N_{FS} , demonstrating oscillating populations. First, the launch and $\Delta J = \pm 1$ states show an immediate onset of oscillatory behavior, with a phase shift between the two, and the oscillations for the $\Delta J = \pm 2$ and ± 3 states show a delayed onset of oscillations. This approximately means that starting with $\Delta J = 0$, population goes to $\Delta J = \pm 1$, then to $\Delta J = 0, \pm 2$, then to $\Delta J = \pm 1, \pm 3$, etc., all via $\Delta J = \pm 1$ transitions. The J states more remote from the launch state (not shown) show a similar delayed onset of population followed by the expected oscillatory behavior. Since all even states are on the A state, and odd states on E, this will produce oscillations in the population between electronic states, with almost complete inversion at high field strengths as all of the even (and odd, respectively) oscillations come into phase at the same field strengths. One interesting observation here is that the oscillation frequency for electronic inversion is twice that for an isolated two state system. Of course, this is easily explainable because in the full model, each state gets depopulated via two channels, namely the P and R branch transitions.

The observed signal is slightly more complicated than a simple observation of populations, since the observable is actually a quantum interference, or coherence, between states that share a common final state[33, 48]. In the experimental system, photoionization occurs via a weak excitation to a narrow band of incoherently autoionizing Rydberg levels, converging on the $v=0$ vibrational state of the ion[47]. Although multiphoton ionization out of the E state has been observed, the primary coherence producing mechanism involves a

single photon. To observe a wave packet, this means that the observed wave packets will have a $\Delta J=2$ component (i.e. $J_E=27$ interfering with $J_E=29$), as these states share the common final state of the average J between the interfering state via the $\Delta J=\pm 1$ single photon ionizing probe, which is accessible by half of the population from each of the interfering states. Similar arguments suggest that the primary wave packets seen on the A state will have a $\Delta J=2$, even though they are photoionized with at least two photons of the probe pulse which has a selection rule of $\Delta J=0, \pm 2$ [6, 94]. As applied to Fig. 6.2, these beats will follow pairs of populations that satisfy the ΔJ interference requirements for a common final state. In an analysis of beat amplitudes as a function of pulse amplitude, the oscillatory behavior will be seen, with beats on the A and E states having a phase shift in their oscillations, like individual populations on the A and E potentials. At lower pulse amplitudes, this behavior will be more complicated, but the qualitative trend remains.

As will be discussed later, the ability to observe wave packet dynamics in the high field requires little dissipation of population within the coupled system of interest. One potential method for minimizing this dissipation is to attenuate wavelengths of light that do not participate in the dynamics that one wants to investigate. For this reason, it is useful to quantify the importance of various spectral contributions to the signal. To perform this, WSS spectra were calculated for a variety of pulse amplitudes in a two level system, shown in Fig. 6.3. The bottom of the figure represents the excited state population as it would appear in our current setup with the sequential attenuation of light on single pixels. As

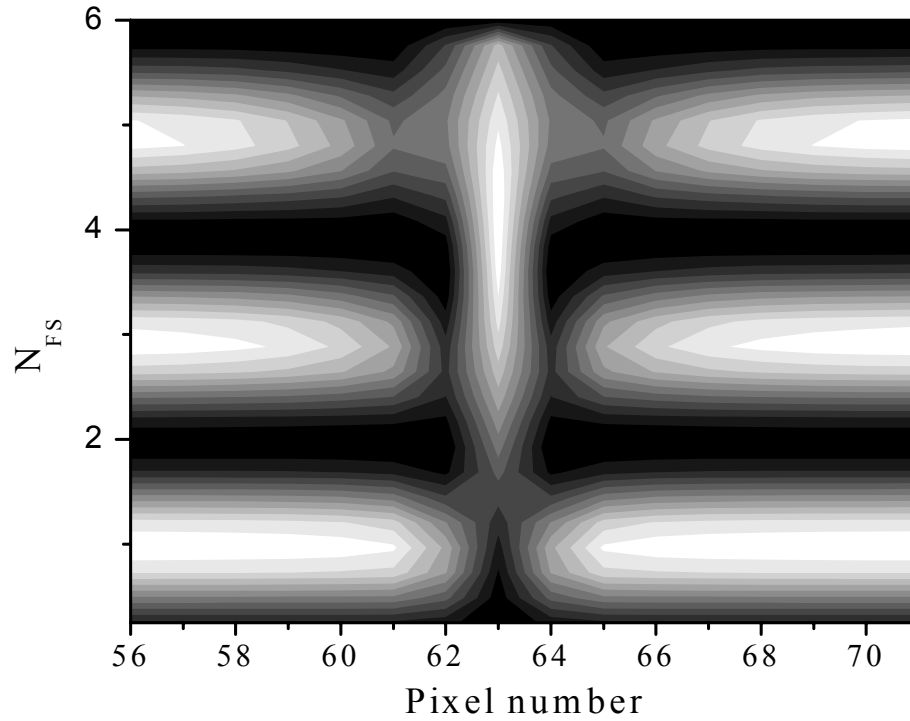


Figure 6.3: Calculated WSS spectrum as a function of normalized field strength for a two level system. Here, N_{FS} is equivalent to the total pulse area multiplied by π . The figure shows the WSS spectrum based on the experimental traits of the pulse shaping setup, with a single resonance centered on pixel 63. White indicates excited state population. The population inversion seen while blocking pixel 63 indicates a nonresonant Rabi oscillation. Note how, at the lowest powers, a notch in the excited state population appears when blocking the pixel 63.

highly nonresonant frequencies are attenuated, we see no significant change in the excited state population: Rabi oscillations in the excited state population are observed. As the resonant frequency is blocked (pixel 63), the population inversion occurs at $N_{FS}=4$ instead of at $N_{FS}=1$, indicating that the Rabi oscillations have a frequency of approximately 8 instead of 2. This is primarily a result of some resonant frequencies being imaged onto pixels adjacent to that where the spectrum is centered. To try to get a more refined sense of what is happening near resonance, sub-pixel resolution on the SLM was assumed. This calculation confirms that at relatively low powers, the population transfer dynamics can be considered almost as resonant processes. Unless the electric field amplitude exceeds 4π , the effective bandwidth for each transition remains below 4 pixels. This suggests the possibility of attenuating frequencies more than 4 pixels from any resonance without concern for significantly changing the energy dependent dynamics. Of course, as should be expected from previous chapters and other published work[6, 8], the highly nonresonant wavelengths become more important if the pulses are phase shaped, as will be addressed in future work not included here.

6.2.2 Alignment effects

An additional mechanism for limiting the visibility of Rabi-type oscillations is attributed to alignment effects, or m_j effects. In all of the calculations in this and the previous section, it was assumed that $m_j=0$, which is not necessarily the case. The presence of multiple m_j states in the initial

wavefunction will result in two different types of effects: dispersion of Rabi oscillation frequencies and a tendency to drive population toward high J . The dispersion of Rabi oscillation frequencies stems from the polarization of the excitation laser. Defining the laboratory coordinate relative to the excitation laser polarization, the transition strength for a parallel transition, such as between the A and E states, decreases as $|m_j|$ increases[92]. In order to study this, the above model was modified to fully account for the presence of multiple m_j states:

$$\Psi(t) = \frac{\sum_{j=-J_0}^{\infty} \sum_{m_j=-j}^j c_j(t) |v_j J_j m_j\rangle}{\sum_{j=-J_0}^{\infty} |c_j(t)|^2} \quad (6.3)$$

where all terms are the same as Eq. (6.1) except the m_j quantum numbers are explicit. The coupled equation scheme of Eq. (6.1c) does not change except that σ_{jk} is further modified by Clebsch-Gordon coefficients coupling the various rotational states. It should be noted that intrinsic to the transition strengths is the requirement that $|m_j| \leq J$, so a transition from $J, m_j=29, 29$ to $J, m_j=28, 29$ has a transition strength of zero, since the 28,29 state does not exist. Since the time or N_{FS} dependence of population evolution show similar dynamics for an unshaped Gaussian pulse (see Fig. 6.2), the time evolution of the population dynamics will be shown here and inferred to reflect the N_{FS} evolution.

If multiple m_j states are populated, there will be multiple m_j dependent Rabi oscillation frequencies, as seen in Fig. 6.4. Shown is the evolution of the launch state population for three selected m_j from a uniform distribution of m_j states under an excitation by a field with N_{FS} equal to 2 with the transition dipole moment and electric field polarizations parallel to $m_j=0$. At short times, all m_j

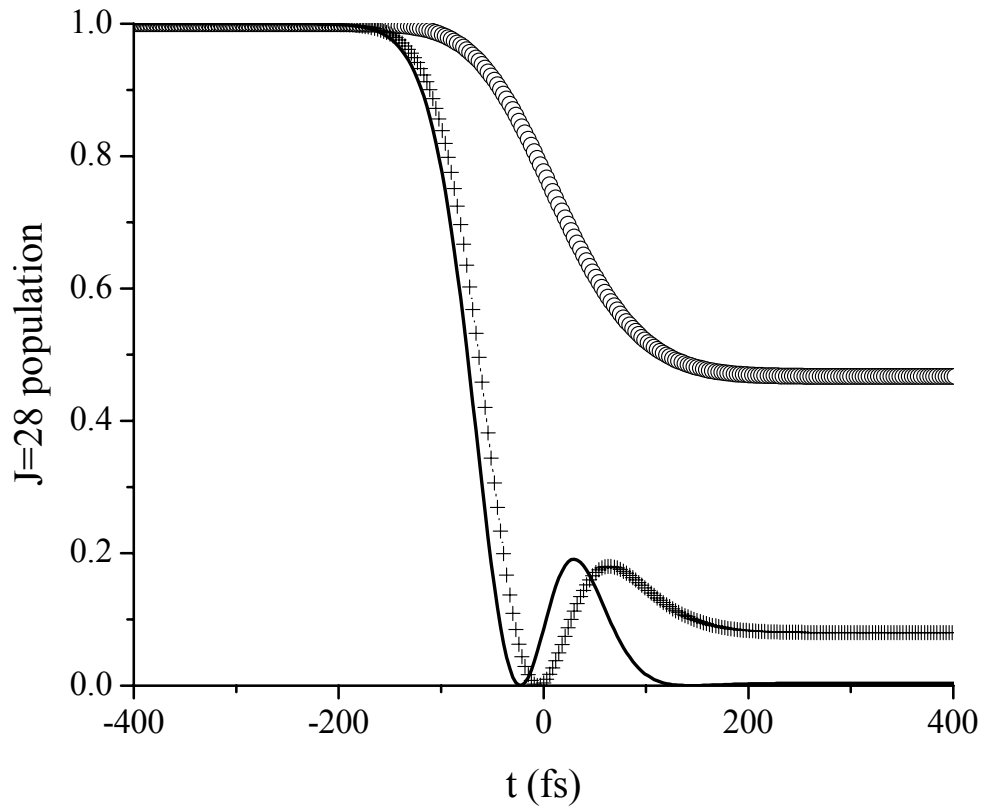


Figure 6.4: Evolution of $J=28$ population for various m_J states under excitation with a laser field with $N_{FS}=2$. m_J quantum numbers of 0, 14, and 28 are represented as the solid line, (+) and (O), respectively.

states are equally populated, but at longer times the m_J distribution clearly deviates from uniform. To describe the nature of the evolution of the m_J distribution, a measure of alignment (Al) for a specific J follows:

$$Al_J(t) = \frac{\sum_{m_J} m_J |c_{J,m_J}(t)|^2}{J \sum_{m_J} |c_{J,m_J}(t)|^2} \quad (6.4)$$

where the $c_{J,m_J}(t)$ coefficients describe J , m_J states, and the J in the denominator is included since the approximate angle of a single m_J state depends on J . Assuming that the total observed population is an incoherent sum of m_J states, the presence of this distribution will reduce the depth of modulation of any observed Rabi-type oscillations and cause the molecules to come into and out of alignment as a function of time or N_{FS} [89, 90].

Figure 6.5 summarizes the population evolution as a function of time for $J=28$ and $N_{FS}=2$. In Fig. 6.5a, the limiting case of a uniform m_J distribution case shows a significant decrease ($\sim 20\%$) in the observed depth of modulation of the oscillations in population. In experiment, the cw and probe lasers are most sensitive to small $|m_J|$ for the same reasons cited above, in effect sampling small $|m_J|$, so the calculation was also performed assuming an additional alignment inducing laser. The time dynamics of the $J=28$ population initially prepared by a weak field cw launch laser shows a depth of modulation of $\sim 95\%$ of the $m_J=0$ case, also shown in Fig. 6.5a. A second weighting laser (such as an ultrafast probe) will further sample small $|m_J|$, but subsequent calculations take a conservative approach and assume a single m_J sampling laser. Pulse shaping strategies can be put into effect to account for this effective spread in m_J dependent transition strengths, and they will be analyzed in section 6.3.2.

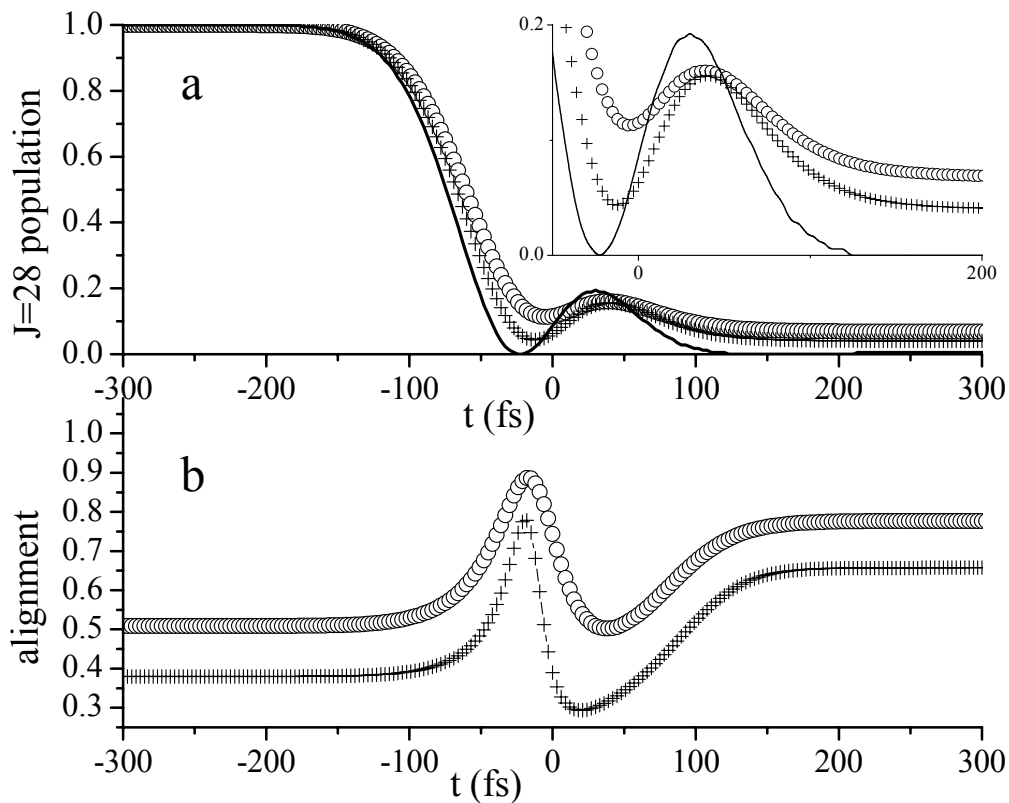


Figure 6.5: Effects of alignment on total population in $J=28$ state. Panel a: total $J=28$ population as a function of time for $N_{FS}=2$. Circles represent the population with a uniform distribution of m_J starting states. Pluses represent the $J=28$ population assuming the presence of a mechanism that samples the m_J space—such as a single weak probe pulse. The solid line shows the evolution of the $m_J=0$ state. All populations have been normalized to a starting population of 1. The inset expands the peak around $t=50$ fs. Panel b: alignment as a function of time for $J=28$ state. Circles and pluses indicate the same conditions as in panel a. In the sampled case, the alignment more closely approaches zero, which is explained by preferentially sampling low $|m_J|$ states. The peaks around -20 fs represent times when population has been transferred out of the low $|m_J|$ states, leaving primarily high $|m_J|$.

In accounting for the total m_j distribution, an interesting alignment trait comes out of the calculation. Consider the $J=28$ launch state, for example. Early in the evolution of its population, the first $|m_j|$ states to be taken out of its total population will be parallel small, leaving large $|m_j|$, as is shown in Fig. 6.5b. For $N_{FS}=2$, the alignment, as defined by Eq. (6.4), goes through a maximum at $t=-20$ fs, in effect creating an incoherent rotation, or wobble, as the incoherent sum of m_j states oscillates between a parallel and perpendicular net alignment. Even in the presence of a low $|m_j|$ weighting laser that preferentially aligns the population parallel to the laser polarization, this wobble still exists at short times.

Alignment effects can also influence the preferred direction ($+J$ instead of $-J$) of a transition with linear laser polarization, since we expect a selection rule of $\Delta m_j=0$. Given this selection rule and the basic degeneracy limitation that $|m_j|\leq J$, choosing a launch state of $J=28$ imposes the condition that $|m_j|\leq 28$ for $J\geq 28$ and $|m_j|\leq J$ for $J<28$, referred to here as population “degeneracy filtering”. Figure 6.6 shows that high J states are favored in this rotational system due to these degeneracy effects using spatially uniform pulses. The time dynamics for the $\Delta J=\pm 3$ (*i.e.* $J=25\&31$) states under excitation with an $N_{FS}=2$ pulse is shown in Fig. 6.6a, with the $J=25:J=31$ population ratio equaling 0.81. This ratio is very close to the ratio of the J state degeneracies between the states, but it should be noted that the population ratio does not rigorously have to match the ratio of J state degeneracies. For example, after excitation using $N_{FS}=2$ the $+\Delta J:-\Delta J$ population ratios for the $\Delta J= \pm 1, \pm 2, \pm 3, \pm 4, \pm 5, \pm 7$ states are 0.97, 0.95, 0.81, 0.90, 0.98,

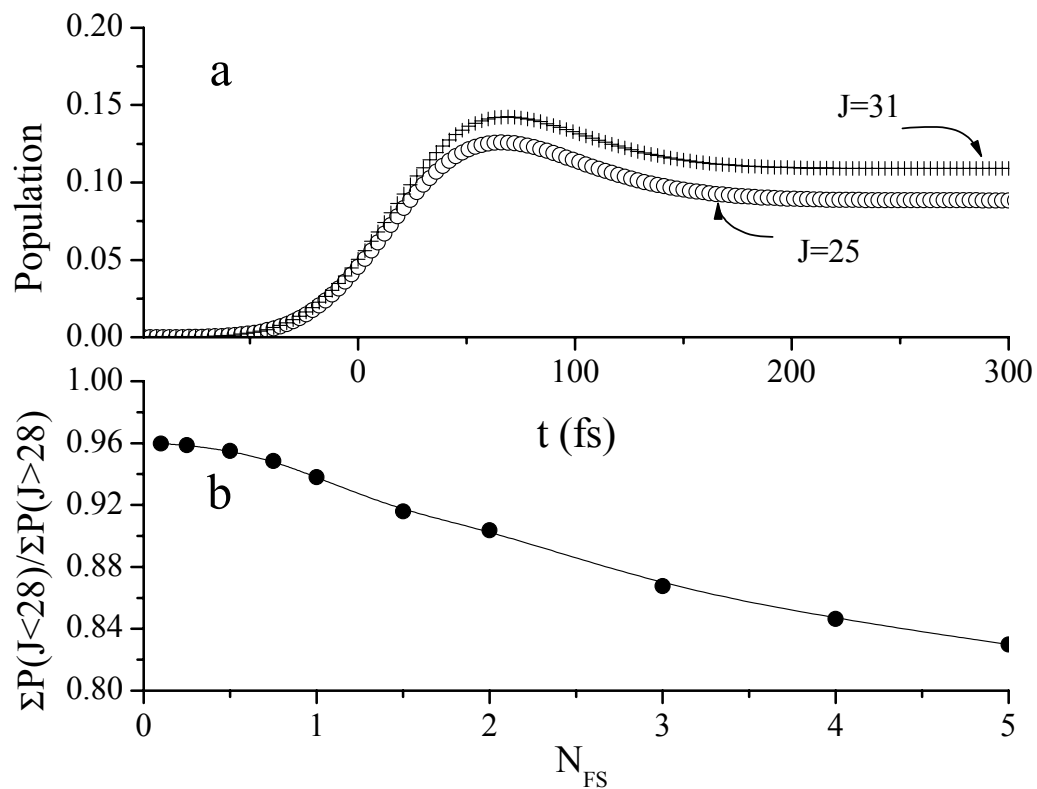


Figure 6.6: Degeneracy dependent selectivity for high J vs low J . Panel a: population evolution for $J=25$ (\circ) and $J=31$ ($+$) for a pulse amplitude with $N_{FS}=2$ and an initially uniform m_j . The final $J=25:J=31$ population ratio is about 0.8. Panel b: Ratio of the sum of all J state populations below the launch state versus those above the launch state as a function of pulse amplitude N_{FS} .

0.98, and 0.94, respectively. This deviation is primarily a result of the fact that this degeneracy filtering is occurring where $|m_j|$ is large, and hence has a relatively weak transition probability. As the optical transitions become stronger, the population ratio for those states with low J versus high J will decrease $[\Sigma(J<28):\Sigma(J>28)]$, as shown in Fig. 6.6b. Plotted is the ratio of the sums of populations for $J<28$ versus $J>28$, where it is shown that increasing N_{FS} increases the selectivity to higher J . In the figure, the low to high J ratio for low N_{FS} approaches .965 and reaches 0.84 at $N_{FS}=5$. At lower N_{FS} , the ratio is fairly insensitive to changes in the field amplitude since the primary states to be involved in a transition will have small $|m_j|$. The ratio of low to high J approaches the average ratio of degeneracies between the low and high J states, 0.75, only at the highest powers. This can only occur in a system that can be saturated, such as this case of a 15 J state model, illustrating a limitation of this model at the highest powers. In the experimental system, since J can approach infinity, saturation will not occur, so the ratio of populations will remain above the ratio of J state degeneracy. Additionally, our experimental laser fields only approach the equivalent of $N_{FS}\sim 2$, reducing the importance of this effect.

6.2.3 Spatially Inhomogenous Fields

In the above analysis, a single value of N_{FS} represents the strength of the electric field. In experimental situations, a single value often fails to describe the electric field[88]. In a typical case, the laser beam used to excite any transition is not uniform, rather spatially Gaussian. In our gas phase sample, the nonuniform

beam excites molecules in different regions of space. The molecules respond as if the excitation comes from a number of independent lasers with varying powers since the molecules are basically uncorrelated with respect to our method of signal detection. For this reason, the spatial extent of our laser beam will be made explicit in further calculations. Since our signal is a result of a pump-probe process, the excitation produced by the pump laser gets spatially sampled by the non-uniform probe pulse, so that pulse will be included in the calculations.

The spatial cross section of a Gaussian beam is described by the following:

$$|\mathcal{E}(R)| = N_{FS} |\mathcal{E}_0| \exp\left[-(2/\ln 2)(R - R_0)^2 / FWHM^2\right] \quad (6.5)$$

where $N_{FS} |\mathcal{E}_0|$ is the normalized electric field amplitude at the center of the beam, the spatial extent R is relative to the center of the beam, and FWHM is the full width at half maximum of the beam radius. This effective field amplitude then gets plugged into Eq. (6.1c) and Eq. (6.2) giving a spatially dependent Rabi frequency. Since the signal has spatial dependence, each of these frequencies gets weighted by a radial factor R . Now the time dependent wave function of Eq. (6.1a) contains an R dependence, and the overall signal is related to it:

$$S(t) \propto \int_R R dR |\text{Pr}(R,t) \Psi(R,t)|^2 \quad (6.6a)$$

$$\Psi(R,t) = \frac{\sum_{j=-J_0}^{\infty} c_j(R,t) |v_j, J_j\rangle}{\sum_{j=-J_0}^{\infty} |c_j(R,t)|^2}, \quad (6.6b)$$

Above, $\text{Pr}(R,t)$ simply refers to a spatial sampling condition fulfilled by the spatially inhomogenous probe pulse, and all summations are relative the launch state $J_0=28$. In this particular subsection, alignment effects will be ignored to

more accurately illustrate spatially specific effects. Additionally, the detected signal is an incoherent integral over R since the ions are detected via an incoherent autoionization of weakly excited Rydberg states[47], so there will be no evidence for spatial coherences in R when taking the modulus squared of the wave function. The R coordinate will only act as a weighting factor.

In experiment, the probe pulse is approximately spatially Gaussian of the same size as the pump, but this assumption carries with it a few caveats. The calculated dependence of the Rabi oscillation visibility versus the size of the beam in the probe step for a two level system is given in Fig. 6.7. In these calculations, the diameter of the probe pulse changes relative to the pump pulse, but the integrated flux remains constant, as if the probe is focused relative to the pump. As the probe size decreases, the observed excited state population behavior evolves from a monotonically increasing type dynamic to a more oscillatory type dynamic. This simply results from sampling a smaller range of field amplitudes of the pump pulse as the probe size decreases. The limit of excitation with a uniform field would look similar to the smallest probe size, except that probe size would not affect depth of modulation of the Rabi oscillations. On the other hand, using a detection scheme that does not sample a small volume in the pump beam would resemble the large probe limit, with virtually no depth of modulation of the N_{FS} dependent Rabi oscillations. An example of such a detection scheme would be in an experiment studying laser induced fluorescence with a single photon excitation.

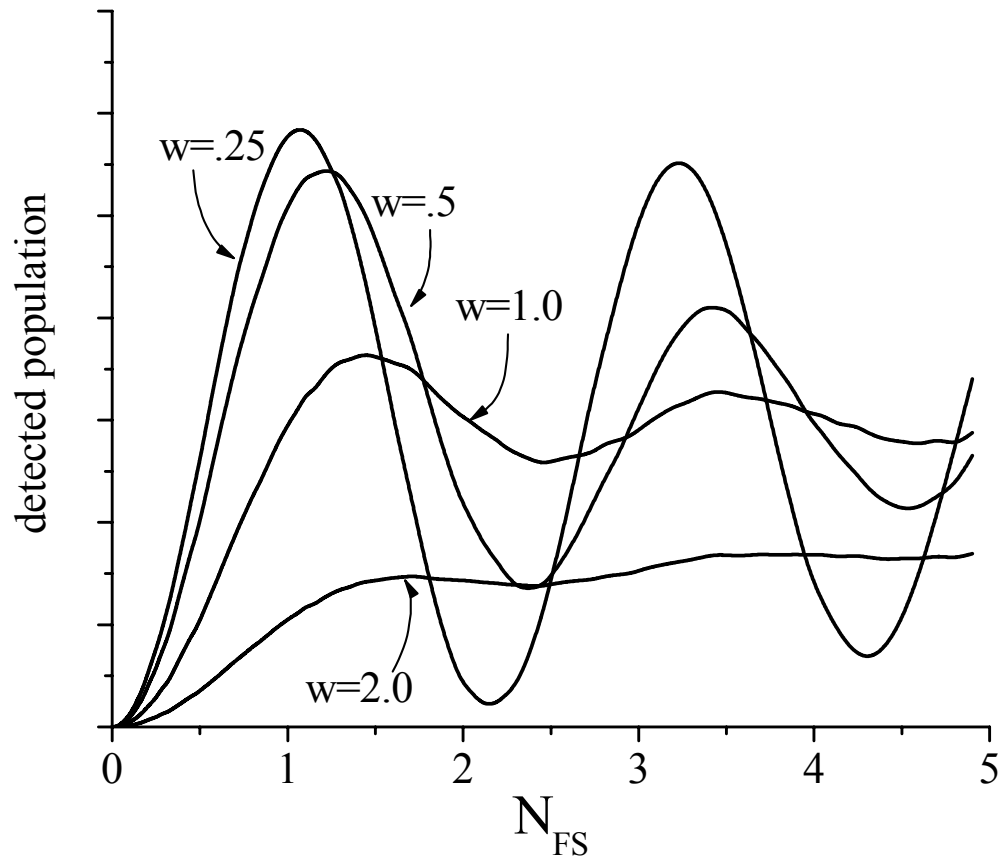


Figure 6.7: Rabi oscillation visibility for various probe sizes. The probe is assumed in all cases to have a constant fluorescence, but changing relative focusing conditions. The detected signal is further assumed to be linear in probe power. The full width at half maximum of the probe is given by w in units of the pump width.

To demonstrate the possibilities for using pulse shapes to control the dynamics of population transfer in this particular system, we examine chirped pulse excitation as a function of N_{FS} . The form of the basic wavefunction now contains aspects of Eq. (6.6b) and Eq. (6.3):

$$\Psi(R,t) = \frac{\sum_{j=-J_0}^{\infty} \sum_{m_j=-j}^j c_j(R,t) |v_{j,J_j,m_j}\rangle}{\sum_{j=-J_0}^{\infty} |c_j(R,t)|^2}, \quad (6.7)$$

where both alignment and beam inhomogeneity effects have been taken into account. In these calculations, an alignment inducing (or m_j sampling) cw laser is assumed. For a probe, a beam with the same spatial extent as the pump is assumed, and a single photon is used to photoionize all E (odd J) states, and two photons are used to photoionize all A (even J) states. In experiment, the A state is photoionized via a two-photon process at approximately 75% of the efficiency of the E state since its signal reflects a smaller sampling region of the excitation region [see Fig. 6.10]. To account for this, the spatially integrated observed population for the A state is set to be 70% of an equally populated E state.

Figure 6.8 shows several states' population dependence on N_{FS} using an excitation pulse with a chirp of 4500 fs². This chirp was chosen for its energetic robustness relative to other chirps not shown here. This figure deviates substantially from the example of excitation with transform limited pulses. First, recurrences in observed populations no longer exist except at fairly high N_{FS} ; instead the population transfers to the $\Delta J=2$ state for a large variety of N_{FS} [86]. In fact, at specific N_{FS} values, there is essentially full population transfer between the launch and final states, but it is not completely visible in the presence of a nonuniform excitation pulse. The populations of the $\Delta J= \pm 1$ states show signature

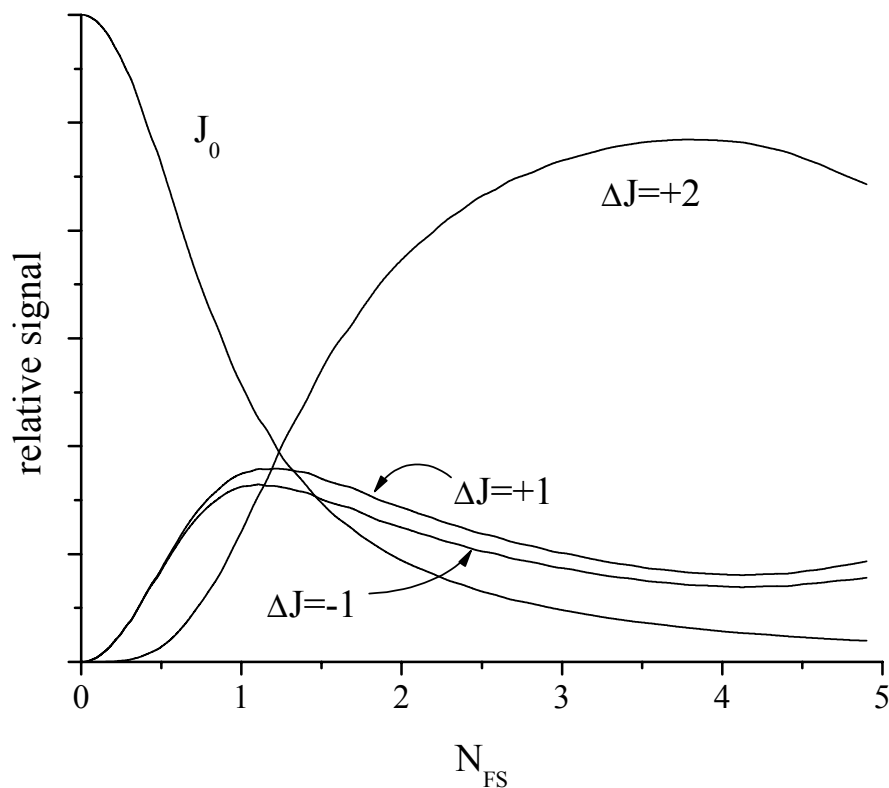


Figure 6.8: Calculated populations as a function of normalized field strength for positively chirped pulse. J_0 indicates the launch state of $J=28$. Note that all even J states lie on the A electronic state and odd lie on the E electronic state. The chirp is set to 4500 fs^5 . The $\Delta J=-2$ state is essentially zero at all N_{FS} . The E (odd) and A (even) states are probed by a beam with the same diameter of pump with 1 and 2 photons, respectively.

dynamics of going through a maximum at fairly low N_{FS} then slowly decaying to near zero, with a small recurrence at very high N_{FS} , and the $\Delta J=-2$ state gets very little population transferred to it at all times shown here. Again, the only reason the $\Delta J=\pm 1$ populations do not go to zero is that the electric field is not uniform. In the case of a uniform electric field, the amplitude of all states except $\Delta J=2$ will go to zero over a wide range of energies. The mechanism behind this energetically robust process is that there are two sequential Rapid Adiabatic Passage events that are separated in time because of the overall chirp of the excitation pulse[52, 66, 71, 72, 78, 86]. This effect has been shown in theory and in atomic excitation where only a single pathway is possible[95], and theoretically with respect to vibrational excitation[81]. Inverting the sign of the chirp will reverse the time ordering of the wavelengths in the pulse, subsequently inverting the Rapid Adiabatic Passage events, giving final state selectivity (not shown).

6.3 Experimental Observations

The goal of this section is to show dissipation of the wave function from a single rotational pair into a much more complex set of states, and then to control the dissipation. Next, it is shown that different quantum beats have different electric field amplitude dependence, reflecting the order of the beats. Finally, a sequential Rapid Adiabatic Transfer dynamical scheme is implemented. Selectivity between final state populations is shown to depend on the sign of the chirp.

To accomplish the experiments described here, the only change to the experimental setup relative to experiments described in previous chapters is that the pump and probe beams pass through a 25 cm focal length lens just at their input to the heat pipe. This gives a spot size of approximately 100 μ m FWHM. For the pump beam, the average power in the heat pipe is approximately 200 mW. Given a pulse duration of approximately 200 fs, and with a repetition rate of 200 kHz, the peak power density is approximately $\sim 10^{11}$ W/cm², several orders of magnitude greater than the weak field experiments described in earlier chapters. As it has been shown in the previous calculations, many of the effects that we expect to observe depend primarily on resonant wavelengths. This allows us to attenuate much of the nonresonant pump light, resulting in a peak power closer to 1×10^{10} W/cm². Still, this intensity will adequately induce Rabi oscillations as described above.

As the power of the pump pulse increases, higher order states become populated at the expense of the population in the launch state. One way of observing this is to identify quantum beats at new frequencies, as summarized in Table 6.1, and shown in Fig. 6.9. In Fig. 6.9, the quantum beat spectrum for two different pump energies using the $J_A=28$ launch state clearly shows the population of a new set of states when the peak pump power increases. The high field trace shows not only the quantum beat between the $J_E=27&29$ states, but also a set of beats between $J_A=28&30$ and $J_E=29&31$. The $J_E=29&31$ beat require at least a third order process to populate the $J_E=31$ state, so its appearance at higher fields

Beat frequency ($\text{cm}^{-1} \pm 0.7 \text{ cm}^{-1}$)	Electronic state	J states	Beat Order*
39.8	E	29-31	4
42.5	E	27-29	2
43.8	A	30-32	6
44.8	E	25-27	4
46.9	A	28-30	2
50.0	A	26-28	2
53.1	A	24-26	6

Table 6.1: $\Delta J=2$ Quantum beat frequencies for $J_A=24$ through 32.

*Beat order is defined as the sum of the $|\Delta J|$ of the states involved in the quantum beat relative to the launch state. From Eq. (6.7), this means that the beat order is defined relative to N_{FS} instead of pulse intensity.

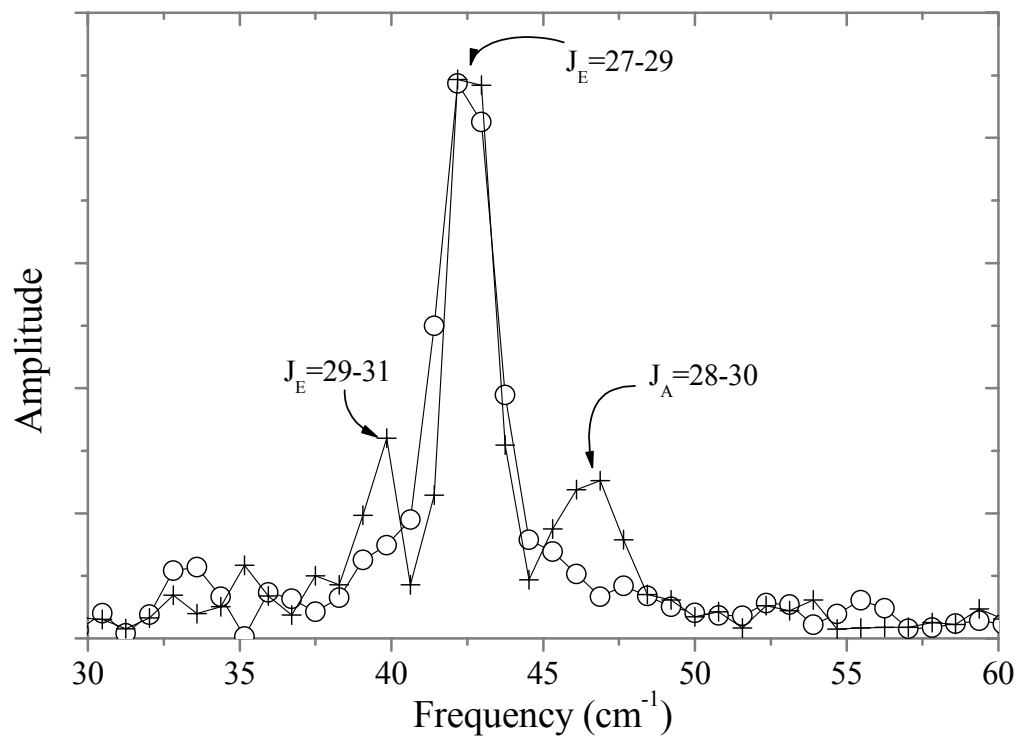


Figure 6.9: Fourier Transforms for quantum beats at two different peak field strengths. The (○) represent the FT for a peak pump power of $\sim 10^8$ W/cm² (unfocused beam), and the (+) represent the FT for a peak pump power of $\sim 10^{11}$ W/cm². Notice the appearance of new beats in the stronger field case. In the low power case, the A state beats were not observed due to insufficient probe power to drive multiphoton ionization. At the high power case here, the low J beats ($J_E=25-27$ and $J_A=26-28$) are minimal due to spectrally weak probe light at the frequencies that photoionize these states, *i.e.* the optimal pulse for $E \leftarrow A$ population transfer is slightly suboptimal for low J photoionization.

should come as no surprise. An additional quantum beat at 44.8 cm^{-1} between $J_E=25&27$ on the E state is sometimes present, but is not observed here for two reasons: the probe spectrum favors the higher J quantum beats, and the beat frequency slightly overlaps the $J_A=28&30$ frequency. Also, the lack of the $J_A=26&28$ beat at 50 cm^{-1} suggests that photoionization yield for low J is small. This occurs here because the wavelength to which the laser is tuned to optimally pump the states of interest is suboptimal for multiphoton ionization of the lower J part of the rotational manifold of states.

Quantum beats that are composed of states excited via high order process will show energy dependent dynamics that vary wildly from linear[66]. The quantum beats as we observe them consist of an interference between two states. As a reminder, the coherence term from Eq. 1.1 has a cosine term with a leading factor that contains the wave function coefficients for each interfering state:

$$\text{Coherence} \propto |p_1 p_2| |c_1| |c_2| \cos(\omega_{12} t + \phi) \quad (6.7)$$

where all terms have been previously defined. Of particular interest is the relationship between the coefficients c_n and the electric field amplitude. In the weak field, first, second, third, etc. order processes are related to the electric field to the first, second, third, etc. power. The quantum beat for a pair of first order states (i.e. $J_E=27-29$) goes as the electric field squared, so it is considered a second order beat. The primary type of quantum beat with the launch state on the A state will also go as the electric field squared, since it involves a product of a second order and a zero order state, giving a net second order process. As the transition strength moves out of the weak field, these simple assumptions become more

difficult to apply. Figure 6.10 shows the quantum beat amplitudes for three types of beats as a function of pulse amplitude.

To gather this data, first the spectrum was manipulated so that the only light to pass through the SLM was a narrow band of $\pm 8 \text{ cm}^{-1}$ around each resonance between the $J_A=28$ and $J_E=27$ and 29 states, enough bandwidth to encompass all first, second, and third order transitions [see Fig. 6.1b]. Next, the bandwidth allowed to pass was attenuated, and a pump-probe trace was taken for each pump intensity. Next, we performed a Fourier Transform of the time-dependent signal. The 42 cm^{-1} beat ($J_E=27\&29$) shows an initial rise followed by a longer decay with a recurrence at the highest N_{FS} . The 47 cm^{-1} ($J_A=28\&30$) beat shows similar behavior, except it shows no recurrence at the highest energies. If both of these beats are second order processes, they should follow the same trajectories vs. N_{FS} at the lowest powers. A third beat at 39 cm^{-1} ($J_E=29\&31$) is shown in the figure. This beat clearly differs from the first two, verifying that this is indeed a fourth order beat as defined in Table 6.1. It shows a threshold at which the quantum beat appears, much like the threshold behavior of calculated third order populations in Fig. 6.2. At the point where the quantum beat appears, significant population has departed from the state of $J_A=30$ to create the third order ($J_E=31$) state.

The fact that the fourth order quantum beat starts to approach the same amplitude as the second order beats suggests that it is being produced in parts of the laser beam where the pulse area approaches 2π (see Fig. 6.7). This observation suggests that pulse shaping schemes may be applied to the system in

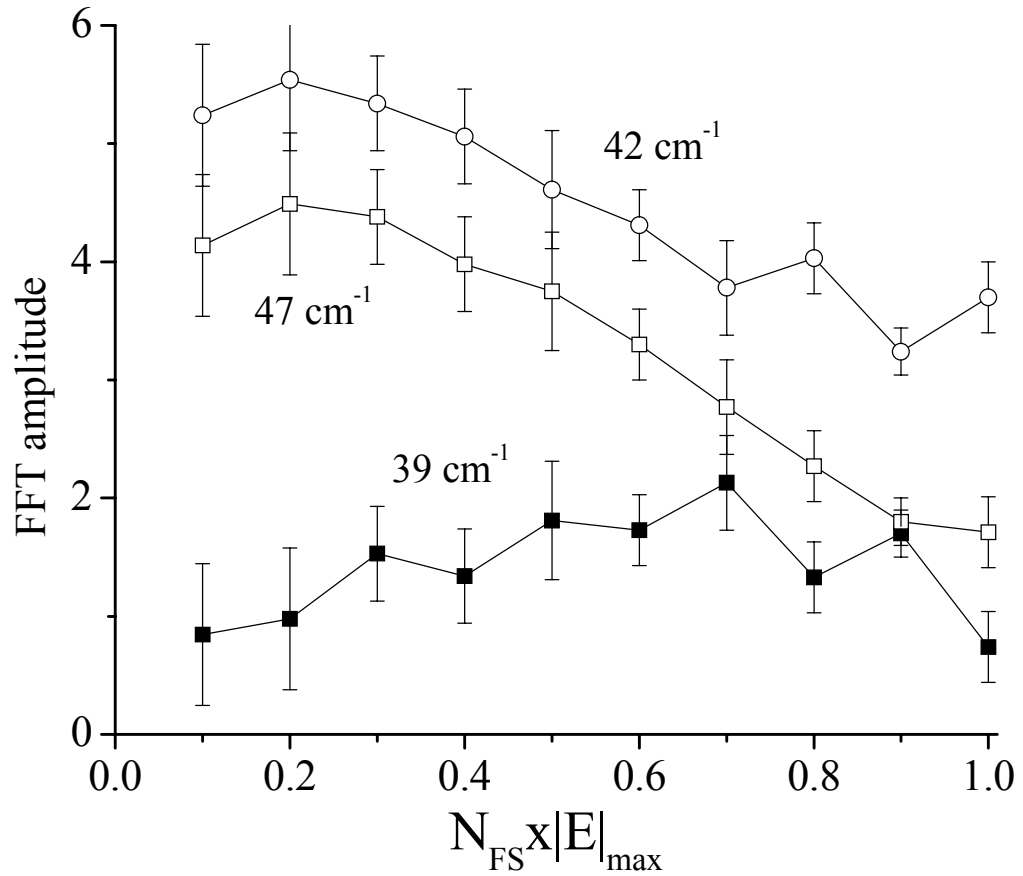


Figure 6.10: Field strength dependence of quantum beat amplitudes. A spectrum containing only first order resonances ($\omega_{\pm 1} \pm 8 \text{ cm}^{-1}$) and nearby wavelengths was created by attenuating all light except for one window four pixels wide around each first order resonance. The relative electric field amplitude dependence of the quantum beats was then recorded. The 42 cm^{-1} , 47 cm^{-1} , and 39 cm^{-1} beats correspond to the coherences between $J_E=27-29$, $J_A=28-30$, and $J_E=29-31$, respectively.

order to control the population transfer to various states. To test the degree to which the populations can be transferred through the first order states, a sequential Rapid Adiabatic Passage pulse shape was tested[95]. To perform this test, the input pulse was attenuated outside a band that contained all of the resonant transitions [see Fig. 6.11]. The light that was able to pass was chirped by the application of a quadratic phase in the frequency domain. The net chirp amounted to $\pm 4500 \text{ fs}^2$, as in the calculation of Fig. 6.11.

The result of the application of this pulse is illustrated in Fig. 6.12. Figure 6.12a shows a Fourier Transform of the recurrence signal for a pulse with zero phase as well as for positively and negatively chirped pulses; all traces have the same intensity spectrum. The unshaped case shows second and fourth order beating. In contrast, the positively chirped case shows a very large quantum beat corresponding to a second order beat ($J_A=28\&30$). Also observed is a sixth order beat ($J_A=30\&32$) at 43.75 cm^{-1} . The second order $J_E=27\&29$ beat is almost completely attenuated, indicating that the second (and fourth) order *states* are populated at the expense of the first order *states*. Here, the beat at 46.9 cm^{-1} is identified as an A state beat since there is a large beat involving the $\Delta J=32$ state, which is very far removed in J space from the $J=25$ state involved in the E state

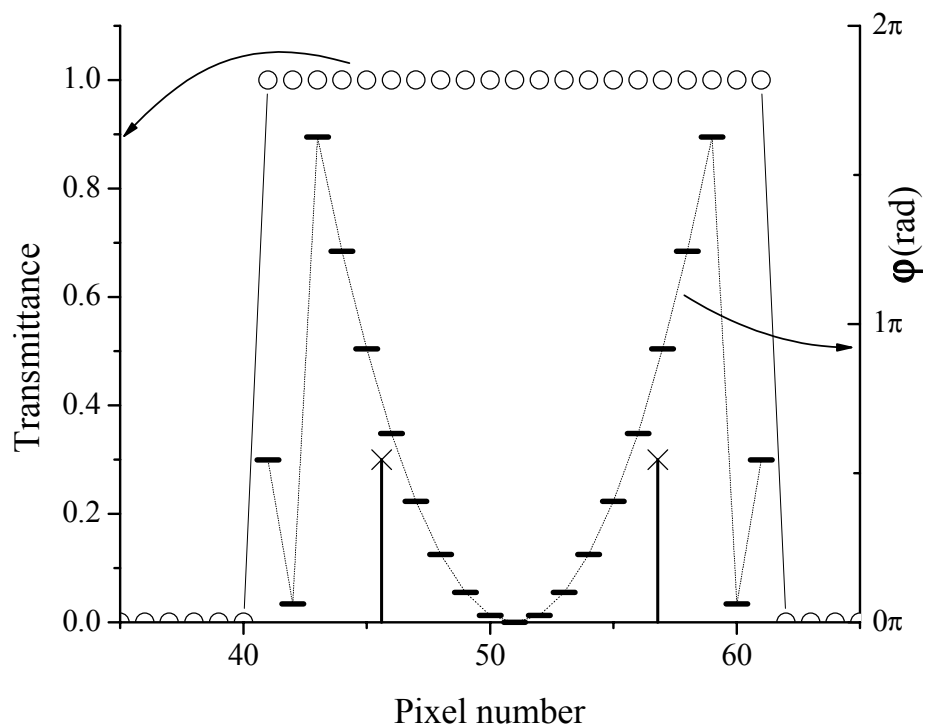


Figure 6.11: Phase and amplitude mask used to induce sequential rapid adiabatic passage events. A window of 84 cm^{-1} , centered to encompass all resonances up to 6th order, allowed light to pass through the pulse shaper (○). Within that window, a chirp of 4500 fs^2 was applied (—). First order resonances are marked (×).

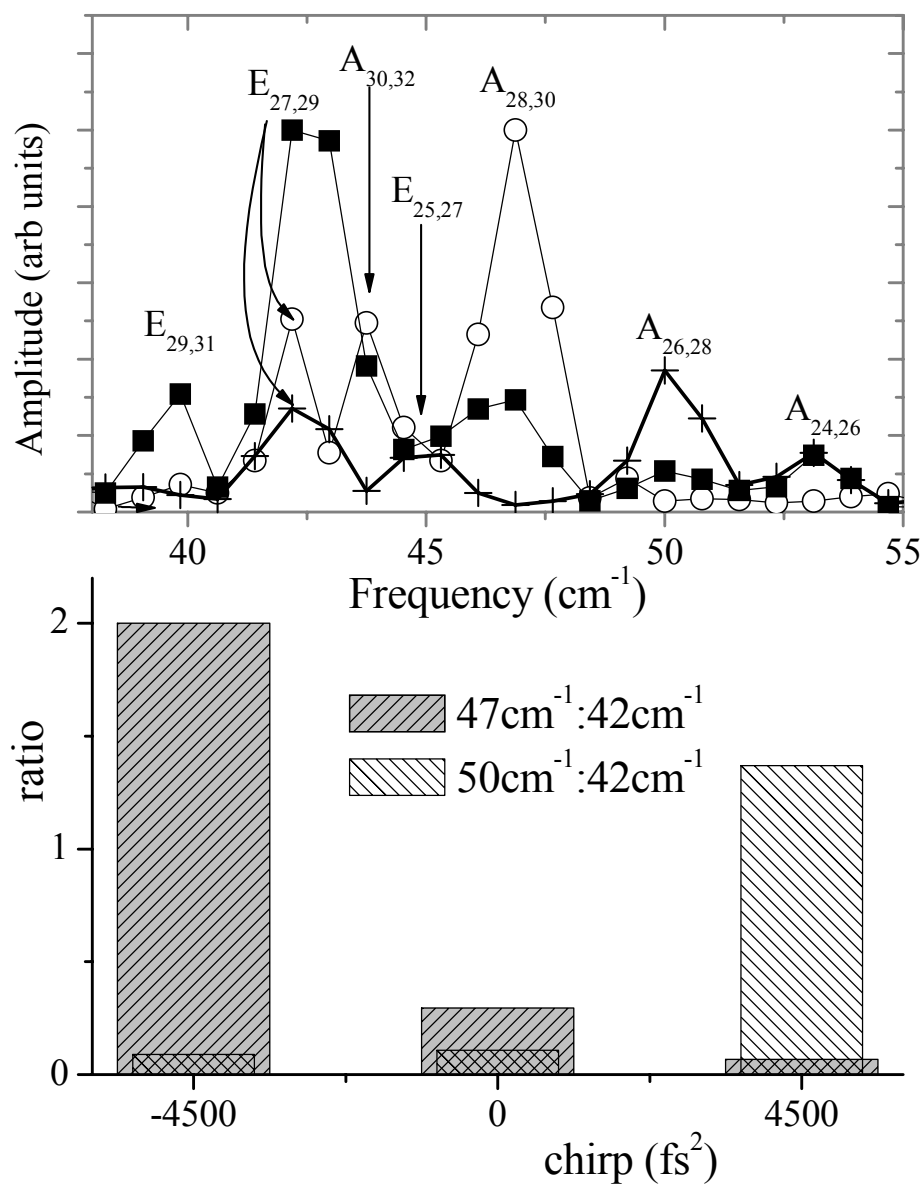


Figure 6.12: Implementation of Raman state selectivity based on the sign of chirp. Panel a: Fourier Transform of quantum beats for non-phase-shaped pulse (■), positively chirped pulse (○), and negatively chirped pulse (+). Quantum beats are labeled by their electronic state, as well as the J state quantum numbers. Panel b: Ratio of A state beats and the E state beat at 42 cm^{-1} . In both chirped cases, the ratio of A state beats is measured to be greater than 20, and is limited by the signal to noise ratio.

beat also at 44.8 cm^{-1} . Similar results, except with the opposite direction of the J transfer, is seen for negatively chirped pulses. For the negatively chirped case, the E state beat is reduced significantly, but the overall amplitude of the A state quantum beats is also small since the probe wavelength for small J is suboptimal, as in Fig. 6.9.

Fig. 6.12b contains a comparison of the amplitudes of various beats as the sign of the chirp is changed. It is quite clear that changing the sign of the chirp effectively selects the pathway being excited by the sequential Rapid Adiabatic Passage mechanism proposed above, with a selectivity between the Stokes and anti-Stokes quantum beats approaching unity. Also remarkably striking is the fact that the observed ratio of the A state quantum beats relative to the $J_E=(27\&29)$ beat approaches a factor of 2, even in the presence of the nonuniform laser beam. Based on the calculations of Fig. 6.8, this selectivity can only be reached at field strengths above 2π , and even at the maximum the ratio in the calculations only reaches 5. This number should be even lower in the experimental situation, since the A state beats are detected via a two-photon ionization, as opposed to the first order photoionization of the first order beats.

In addition to the ladder climbing technique described above, another technique has been developed by other groups that shows a high degree of robustness with respect to power: STIRAP[79]. In the STIRAP Λ excitation scheme—where there are two ground states and one excited state (e.g. only $J_A=28$ & 30, $J_E=29$ in the above model)—the three level system is “dressed” by two resonant excitation sources corresponding to the pump and dump frequencies. In

the case where the dump frequency slightly *precedes* the pump frequency, robust excitation of the Stokes state is seen. Unfortunately, in this experimental system, the dump then pump pulse order that corresponds to the excitation of the $\Delta J=2$ state is nearly identical to the pump then dump excitation to $\Delta J=-2$. This pathway ambiguity prevents the implementation of STIRAP in the previously described rotational system.

In these experiments, the degree of population transfer is not the observed quantity. Instead, the observed characteristics are coherences between states, as in Eq. (6.7); if all population were transferred to a single state, then the coherence would be zero. Still, it can be tentatively concluded that *most* of the population is transferred to the $\Delta J=\pm 2$ states as a result of the large amplitude of the second and sixth order beats. Also, the good agreement with the theoretical mechanism supports the conclusion that most population finds its way to the target states. Further experiments that are sensitive to individual populations, such as fluorescence detection, will verify these final state populations. One expected loss in quality of data by using fluorescence detection is the probe pulse beam sampling effect, as described in Eq. (6.7) will be lost. This can be overcome by carefully creating a spatially uniform electric excitation field, or by using a variant of Stimulated Emission Pumping to detect final state populations.

These experiments can also be improved by more carefully selecting the chemical system being studied to minimize loss mechanisms such as pump pulse multiphoton ionization. An attempt to overcome this in our current experiment by attenuating nonresonant wavelengths in the pump has shown some promise, but

more study is necessary to fully characterize the spectral extent to all multiphoton ionization pathways. We have shown that quantum beat amplitudes can be increased by up to 70% by attenuating nonresonant frequencies. A potential solution could be to perform these experiments on a system with a much higher ionization potential, or even to lower the energy of the launch state so that an additional photon of light is needed to reach the ionization continuum.